

Fast Single Image Super-resolution using a New Analytical Solution for $\ell_2 - \ell_2$ Problems

Ningning Zhao, Qi Wei, Adrian Basarab, Nicolas Dobigeon, Denis Kouamé
and Jean-Yves Tourneret

Abstract

This paper addresses the problem of single image super-resolution (SR), which consists of recovering a high resolution image from its blurred, decimated and noisy version. The existing algorithms for single image SR use different strategies to handle the decimation and blurring operators. In addition to the traditional first-order gradient methods, recent techniques investigate splitting-based methods dividing the SR problem into up-sampling and deconvolution steps that can be easily solved. Instead of following this splitting strategy, we propose to deal with the decimation and blurring operators simultaneously by taking advantage of their particular properties in the frequency domain, leading to a new fast SR approach. Specifically, an analytical solution can be obtained and implemented efficiently for the Gaussian prior or any other regularization that can be formulated into an ℓ_2 -regularized quadratic model, i.e., an ℓ_2 - ℓ_2 optimization problem. Furthermore, the flexibility of the proposed SR scheme is shown through the use of various priors/regularizations, ranging from generic image priors to learning-based approaches. In the case of non-Gaussian priors, we show how the analytical solution derived from the Gaussian case can be embedded into traditional splitting frameworks, allowing the computation cost of existing algorithms to be decreased significantly. Simulation results conducted on several images with different priors illustrate the effectiveness of our fast SR approach compared with the existing techniques.

Part of this work has been supported by the Chinese Scholarship Council and the thematic trimester on image processing of the CIMI Labex, Toulouse, France, under grant ANR-11-LABX-0040-CIMI within the program ANR-11-IDEX-0002-02.

Ningning Zhao, Nicolas Dobigeon and Jean-Yves Tourneret are with University of Toulouse, IRIT/INP-ENSEEIH, 31071 Toulouse Cedex 7, France (e-mail: {nzhao, nicolas.dobigeon, jean-yves.tourneret}@enseeih.fr).

Qi Wei is with Department of Engineering, University of Cambridge, CB21PZ, U.K. (e-mail: {qw245}@cam.ac.uk).

Adrian Basarab and Denis Kouamé are with University of Toulouse, IRIT, CNRS UMR 5505, 118 Route de Narbonne, F-31062, Toulouse Cedex 9, France (e-mail: {adrian.basarab, denis.kouame}@irit.fr).

Index Terms

Single image super-resolution, deconvolution, decimation, block circulant matrix, variable splitting based algorithms.

I. INTRODUCTION

Single image super-resolution (SR), also known as image scaling up or image enhancement, aims at estimating a high-resolution (HR) image from a low-resolution (LR) observed image [1]. This resolution enhancement problem is still an ongoing research problem with applications in various fields, such as remote sensing [2], video surveillance [3], hyperspectral [4], microwave [5] or medical imaging [6].

The methods dedicated to single image SR can be classified into three categories [7]–[9]. The first category includes the interpolation based algorithms such as nearest neighbor interpolation, bicubic interpolation [10] or adaptive interpolation techniques [11], [12]. Despite their simplicity and easy implementation, it is well-known that these algorithms generally over-smooth the high frequency details. The second type of methods consider learning-based (or example-based) algorithms that learn the relations between LR and HR image patches from a given database [7], [13]–[16]. Note that the effectiveness of the learning-based algorithms highly depends on the training image database and these algorithms have generally a high computational complexity. Reconstruction-based approaches that are considered in this paper belong to the third category of SR approaches [8], [9], [17], [18]. These approaches formulate the image SR as an reconstruction problem, either by incorporating priors in a Bayesian framework or by introducing regularizations into the ill-posed inverse problem.

Existing reconstruction-based techniques used to solve the single image SR include the first order gradient-based methods [7]–[9], [17], the iterative shrinkage thresholding-based algorithms [19] (also called forward-backward algorithms), proximal gradient algorithms and other variable splitting algorithms that rely on the augmented Lagrangian (AL) scheme. The AL based algorithms include the alternating direction method of multipliers (ADMM) [2], [6], [18], [20], split Bregman (SB) methods [5] (known to be equivalent to ADMM in certain conditions [21]) and their variants.

Particularly, Ng *et. al.* [18] proposed an ADMM-based algorithm to solve a TV-regularized single image SR problem, where the decimation and blurring operators are split and solved iteratively. Due to this splitting, the cumbersome SR problem can be decomposed into an up-sampling problem and a deconvolution problem, that can be both solved efficiently. Yanovsky *et. al.* [5] proposed to solve the same problem with an SB algorithm. However, the decimation operator was handled through a gradient descent method integrated in the SB framework. Sun *et. al.* [8], [17] proposed a gradient profile prior and formulated the single image SR problem as an ℓ_2 -regularized optimization problem, further solved with the gradient descent method. Yang *et. al.* [7] proposed a learning-based algorithm for the single image SR by seeking a sparse representation using the patches of LR and HR images, followed by back projecting through a gradient descent method. Despite the efficiency of these methods, it is still appealing to deal with the single image SR problem in a non-iterative or more efficient way.

This paper aims at reducing the computational cost of these methods by proposing a new approach handling the decimation and blurring operators simultaneously by exploring their intrinsic properties in the frequency domain. It is interesting to note that similar properties were explored in [22], [23] for multi-frame SR. However, the implementation of the matrix inversions proposed in [22], [23] are less efficient than those proposed in this work, as it will be demonstrated in the complexity analysis conducted in Section III. More precisely, this paper derives a closed-form expression of the solution associated with the ℓ_2 -penalized least-squares SR problem, when the observed LR image is assumed to be a noisy, subsampled and blurred version of the HR image with a spatially invariant blur. This model, referred to as $\ell_2 - \ell_2$ in what follows, underlies the restoration of an image contaminated by additive Gaussian noise and has been used intensively for the single image SR problem, see, e.g., [7], [8], [24] and the references mentioned above. The proposed solution is shown to be easily embeddable into an AL framework to handle non-Gaussian priors (i.e., non- ℓ_2 regularizations), which significantly lightens the computational burdens of several existing SR algorithms.

The remainder of the paper is organized as follows. Section II formulates the single image SR problem as an optimization problem. In Section III, we study the properties of the down-sampling and blurring operators in the frequency domain and introduce a fast SR scheme

based on an analytical solution of the $\ell_2 - \ell_2$ model, that can be formulated in the image or gradient domains. Section IV generalizes the proposed fast SR scheme to more complex regularizations in image or transformed domains. Various experiments presented in Section V demonstrate the efficiency of the proposed fast single image SR scheme. Conclusions and perspectives are finally reported in Section VI.

II. IMAGE SUPER-RESOLUTION FORMULATION

A. Model of Image Formation

In the single image SR problem, the observed LR image is modeled as a noisy version of the blurred and decimated HR image to be estimated as follows,

$$\mathbf{y} = \mathbf{S}\mathbf{H}\mathbf{x} + \mathbf{n} \quad (1)$$

where the vector $\mathbf{y} \in \mathbb{R}^{N_l \times 1}$ ($N_l = m_l \times n_l$) denotes the LR observed image and $\mathbf{x} \in \mathbb{R}^{N_h \times 1}$ ($N_h = m_h \times n_h$) is the vectorized HR image to be estimated, with $N_h > N_l$. The vectors \mathbf{y} and \mathbf{x} are obtained by stacking the corresponding images (LR image $\in \mathbb{R}^{m_l \times n_l}$ and HR image $\in \mathbb{R}^{m_h \times n_h}$) into column vectors in a lexicographic order. Note that the vector $\mathbf{n} \in \mathbb{R}^{N_l \times 1}$ is an independent identically distributed (*i.i.d.*) additive white Gaussian noise (AWGN) and that the matrices $\mathbf{S} \in \mathbb{R}^{N_l \times N_h}$ and $\mathbf{H} \in \mathbb{R}^{N_h \times N_h}$ represent the decimation and the blurring/convolution operations respectively. More specifically, \mathbf{H} is a block circulant matrix with circulant blocks, which corresponds to cyclic convolution boundaries, and left multiplying by \mathbf{S} performs down-sampling with an integer factor d ($d = d_r \times d_c$), i.e., $N_h = N_l \times d$. The decimation factors d_r and d_c represent the numbers of discarded rows and columns from the input images satisfying the following relationships $m_h = m_l \times d_r$ and $n_h = n_l \times d_c$. Note that the image formation model (1) has been widely considered in single image SR problems, see, e.g., [7], [8], [17], [18], [25].

We introduce two additional basic assumptions about the blurring and decimation operators. These assumptions have been widely used for image deconvolution or image SR problems (see, e.g., [7], [16], [26], [27]) and are necessary for the proposed fast SR framework.

Assumption 1. *The blurring matrix \mathbf{H} is the matrix representation of the cyclic convolution operator, i.e., \mathbf{H} is a block circulant matrix with circulant blocks (BCCB).*

This assumption has been widely resorted in the image processing literature [22], [23], [28]. It is satisfied provided the underlying blurring kernel is shift-invariant and the boundary conditions make the convolution operator periodic. Note that the BCCB matrix assumption does not depend on the shape of the blurring kernel, i.e., it is satisfied for any kind of blurring, including motion blur, out-of-focus blur, atmospheric turbulence, etc. Using the cyclic convolution assumption, the blurring matrix and its conjugate transpose can be decomposed as

$$\mathbf{H} = \mathbf{F}^H \mathbf{\Lambda} \mathbf{F} \quad (2)$$

$$\mathbf{H}^H = \mathbf{F}^H \mathbf{\Lambda}^H \mathbf{F} \quad (3)$$

where the matrices \mathbf{F} and \mathbf{F}^H are associated with the Fourier and inverse Fourier transforms (satisfying $\mathbf{F}\mathbf{F}^H = \mathbf{F}^H\mathbf{F} = \mathbf{I}_{N_h}$) and $\mathbf{\Lambda} = \text{diag}\{\mathbf{F}\mathbf{h}\} \in \mathbb{C}^{N_h \times N_h}$ is a diagonal matrix, whose diagonal elements are the Fourier coefficients of the first column of the blurring matrix \mathbf{H} , denoted as \mathbf{h} . Using the decompositions (2) and (3), the blurring operator $\mathbf{H}\mathbf{x}$ and its conjugate $\mathbf{H}^H\mathbf{x}$ can be efficiently computed in the frequency domain, see, e.g., [29]–[31].

Assumption 2. *The decimation matrix $\mathbf{S} \in \mathbb{R}^{N_l \times N_h}$ is a down-sampling operator, while its conjugate transpose $\mathbf{S}^H \in \mathbb{R}^{N_h \times N_l}$ interpolates the decimated image with zeros.*

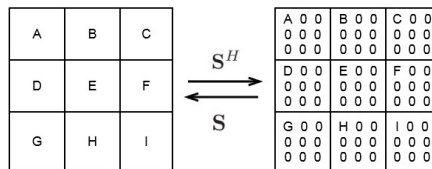


Fig. 1. Effect of the up-sampling matrix \mathbf{S}^H on a 3×3 image and of the down-sampling matrix \mathbf{S} on the corresponding 9×9 image (whose scale up factor equals 3).

Once again, numerous research works have used this assumption [7], [16], [22], [23]. Fig. 1 shows a toy example highlighting the roles of the decimation matrix \mathbf{S} and its conjugate

transpose \mathbf{S}^H . The decimation matrix satisfies the relationship $\mathbf{S}\mathbf{S}^H = \mathbf{I}_{N_l}$. Denoting $\underline{\mathbf{S}} \triangleq \mathbf{S}^H\mathbf{S}$, multiplying an image by $\underline{\mathbf{S}}$ can be achieved by making an entry-wise multiplication with an $N_h \times N_h$ mask having ones at the sampled positions and zeros elsewhere.

B. Problem formulation

Similar to traditional image reconstruction problems, the estimation of an HR image from the observation of an LR image is not invertible, leading to an ill-posed problem. This ill-posedness is classically overcome by incorporating some appropriate prior information or regularization term. The regularization term can be chosen from a specific task of interest, the information resulting from previous experiments or from a perceptual view on the constraints affecting the unknown model parameters [32], [33]. Various priors or regularizations have already been advocated to regularize the image SR problem in the literature include: (i) traditional generic image priors such as Tikhonov [24], [34], [35], the total variation (TV) [18], [20], [36] and the sparsity in transformed domains [37]–[40], (ii) more recently proposed image regularizations such as the gradient profile prior [8], [9], [17] or Fattal’s edge statistics [41] and (iii) learning-based priors [42], [43]. The fast approach proposed in the next section is shown to be adapted to many of the existing regularization terms. Note that proposing new regularization terms with improved SR performance is out of the scope of this paper.

Assuming that the noise \mathbf{n} in (1) is AWGN and incorporating a proper regularization to the target image \mathbf{x} , the maximum *a posteriori* (MAP) estimator of \mathbf{x} for the single image SR can be obtained by solving the following optimization problem

$$\min_{\mathbf{x}} \underbrace{\frac{1}{2} \|\mathbf{y} - \mathbf{S}\mathbf{H}\mathbf{x}\|_2^2}_{\text{data fidelity}} + \tau \underbrace{\phi(\mathbf{A}\mathbf{x})}_{\text{regularization}} \quad (4)$$

where $\|\mathbf{y} - \mathbf{S}\mathbf{H}\mathbf{x}\|_2^2$ is a *data fidelity term* associated with the model likelihood and $\phi(\mathbf{A}\mathbf{x})$ is related to the image prior information and is referred to as *regularization* or *penalty* [44]. Note that the matrix \mathbf{A} can be the identity matrix when the regularization is imposed on the SR image itself, the gradient operator, any orthogonal matrix or normalized tight frame, depending on the addressed application and the properties of the target image. The role of the regularization parameter τ is to weight the importance of the regularization term with

respect to (w.r.t.) the data fidelity term. The next section derives a closed-form solution of the problem (4) for a quadratic regularizing operator $\phi(\cdot)$ when the assumptions 1 and 2 hold.

III. PROPOSED FAST SUPER-RESOLUTION USING AN ℓ_2 -REGULARIZATION

Before proceeding to more complicated regularizations investigated in Section IV, we first consider the basic ℓ_2 -norm regularization defined by

$$\phi(\mathbf{Ax}) = \|\mathbf{Ax} - \mathbf{v}\|_2^2 \quad (5)$$

where the matrix $\mathbf{A}^H \mathbf{A}$ is assumed, unless otherwise specified, to be invertible. Typical examples of matrices \mathbf{A} include the Fourier transform matrix, the wavelet transform matrix, etc. Under this ℓ_2 -norm regularization, a generic form of a fast solution to problem (4) will be derived in Section III-A. Then, two particular cases of this regularization widely used in the literature will be discussed in Sections III-B and III-C.

A. Proposed closed-form solution for the $\ell_2 - \ell_2$ problem

With the regularization (5), the problem (4) transforms to

$$\min_{\mathbf{x}} \frac{1}{2} \|\mathbf{y} - \mathbf{S}\mathbf{H}\mathbf{x}\|_2^2 + \tau \|\mathbf{Ax} - \mathbf{v}\|_2^2 \quad (6)$$

whose solution is given by

$$\hat{\mathbf{x}} = (\mathbf{H}^H \underline{\mathbf{S}}\mathbf{H} + 2\tau \mathbf{A}^H \mathbf{A})^{-1} (\mathbf{H}^H \mathbf{S}^H \mathbf{y} + 2\tau \mathbf{A}^H \mathbf{v}) \quad (7)$$

with $\underline{\mathbf{S}} = \mathbf{S}^H \mathbf{S}$.

Direct computation of the analytical solution (7) requires the inversion of a high dimensional matrix, whose computational complexity is of order $\mathcal{O}(N_h^3)$. One can think of using optimization or simulation-based methods to overcome this computational difficulty. The optimization-based methods, such as the gradient-based methods [17] or, more recently, the ADMM [18] and SB [5] method approximate the solution of (6) by iterative updates. The simulation-based methods, e.g., the Markov Chain Monte Carlo methods [45]–[47], are drawing samples from a multivariate posterior distribution (which is Gaussian for a Tikhonov regularization) and compute the average of the generated samples to approximate

the minimum mean square error (MMSE) estimator of \mathbf{x} . However, simulation-based methods have the major drawback of being computationally expensive, which prevents their effective use when processing large images. Moreover, because of the particular structure of the decimation matrix, the joint operator \mathbf{SH} cannot be diagonalized in the frequency domain, which prevents any direct implementation of the solution (7) in this domain. The main contribution in this work is proposing a new scheme to compute (7) explicitly, getting rid of any statistically sampling or iterative update and leading to a fast SR method.

In order to compute the analytical solution (7), a property of the decimation matrix in the frequency domain is first stated in Lemma 1.

Lemma 1 (Wei *et al.*, [35]). *The following equality holds*

$$\mathbf{F}\mathbf{S}\mathbf{F}^H = \frac{1}{d}\mathbf{J}_d \otimes \mathbf{I}_{N_l} \quad (8)$$

where $\mathbf{J}_d \in \mathbb{R}^{d \times d}$ is a matrix of ones, $\mathbf{I}_{N_l} \in \mathbb{R}^{N_l \times N_l}$ is the $N_l \times N_l$ identity matrix and \otimes is the Kronecker product.

Using the property of the matrix $\mathbf{F}\mathbf{S}\mathbf{F}^H$ given in Lemma 1 and taking into account the assumptions mentioned above, the analytical solution (7) can be rewritten as

$$\hat{\mathbf{x}} = \mathbf{F}^H \left(\frac{1}{d}\underline{\mathbf{\Lambda}}^H \underline{\mathbf{\Lambda}} + 2\tau \mathbf{F}\mathbf{A}^H \mathbf{A}\mathbf{F}^H \right)^{-1} \mathbf{F} (\mathbf{H}^H \mathbf{S}^H \mathbf{y} + 2\tau \mathbf{A}^H \mathbf{v}) \quad (9)$$

where the matrix $\underline{\mathbf{\Lambda}} \in \mathbb{C}^{N_l \times N_h}$ is defined as

$$\underline{\mathbf{\Lambda}} = [\mathbf{\Lambda}_1, \mathbf{\Lambda}_2, \dots, \mathbf{\Lambda}_d] \quad (10)$$

and where the blocks $\mathbf{\Lambda}_i \in \mathbb{C}^{N_l \times N_l}$ ($i = 1, \dots, d$) satisfy the relationship

$$\text{diag}\{\mathbf{\Lambda}_1, \dots, \mathbf{\Lambda}_d\} = \underline{\mathbf{\Lambda}}. \quad (11)$$

The readers may refer to the Appendix A for more details about the derivation of (9) from (7).

To further simplify the expression (9), we propose to use the following Woodbury inverse formula.

Lemma 2 (Woodbury formula [48]). *The following equality holds conditional on the existence of \mathbf{A}_1^{-1} and \mathbf{A}_3^{-1}*

$$\begin{aligned} & (\mathbf{A}_1 + \mathbf{A}_2\mathbf{A}_3\mathbf{A}_4)^{-1} \\ &= \mathbf{A}_1^{-1} - \mathbf{A}_1^{-1}\mathbf{A}_2(\mathbf{A}_3^{-1} + \mathbf{A}_4\mathbf{A}_1^{-1}\mathbf{A}_2)^{-1}\mathbf{A}_4\mathbf{A}_1^{-1} \end{aligned} \quad (12)$$

where \mathbf{A}_1 , \mathbf{A}_2 , \mathbf{A}_3 and \mathbf{A}_4 are matrices of correct sizes.

Taking into account the Woodbury formula of Lemma 2, the analytical solution (9) can be computed very efficiently as stated in the following theorem.

Theorem 1. *When Assumptions 1 and 2 are satisfied, the solution of Problem (6) can be computed using the following closed-form expression*

$$\begin{aligned} \hat{\mathbf{x}} &= \frac{1}{2\tau}\mathbf{F}^H\Psi\mathbf{F}\mathbf{r} \\ &\quad - \frac{1}{2\tau}\mathbf{F}^H\Psi\underline{\mathbf{\Lambda}}^H(2\tau d\mathbf{I}_{N_l} + \underline{\mathbf{\Lambda}}\Psi\underline{\mathbf{\Lambda}}^H)^{-1}\underline{\mathbf{\Lambda}}\Psi\mathbf{F}\mathbf{r} \end{aligned} \quad (13)$$

where $\mathbf{r} = \mathbf{H}^H\mathbf{S}^H\mathbf{y} + 2\tau\mathbf{A}^H\mathbf{v}$, $\Psi = \mathbf{F}(\mathbf{A}^H\mathbf{A})^{-1}\mathbf{F}^H$ and $\underline{\mathbf{\Lambda}}$ is defined in (10).

Proof: See Appendix A. ■

Complexity Analysis

The most computationally expensive part for the computation of (13) in Theorem 1 is the implementation of FFT/iFFT. In total, four FFT/iFFT computations are required in our implementation. Comparing with the original problem (7), the order of computation complexity has decreased significantly from $\mathcal{O}(N_h^3)$ to $\mathcal{O}(N_h \log N_h)$, which allows the analytical solution (13) to be computed efficiently. Note that [22], [23] also addressed image SR problems by using the properties of $\underline{\mathbf{S}}$ in the frequency domain, where N_l small matrices of size $d \times d$ were inverted. The total computational complexity of the methods investigated in [22], [23] is $\mathcal{O}(N_h \log N_h + N_h d^2)$. Another important difference with our work is that the authors of [22] and [23] decomposed the SR problem into an upsampling (including motion estimation which is not considered in this work) and a deblurring step. The operators \mathbf{H} and \mathbf{S} were thus considered separately, thus requiring two ℓ_2 regularizations for the blurred image (referred to as \mathbf{z} in [22]) and the ground-truth image (referred to as \mathbf{x} in [22]). On the contrary, this work

considers the blurring and downsampling jointly and achieve the SR in one step, requiring only one regularization term for the unknown image. It is worthy to mention that the proposed SR solution can be extended to incorporate the warping operator considered in [22], [23], which can also be modelled as a BCCB matrix. This is not included in this paper but will be considered in future work.

In the sequel of this section, two particular instances of the ℓ_2 -norm regularization are considered, defined in the image and gradient domains, respectively.

B. Solution of the $\ell_2 - \ell_2$ problem in the image domain

First, we consider the specific case where $\mathbf{A} = \mathbf{I}_{N_h}$ and $\mathbf{v} = \bar{\mathbf{x}}$, i.e., the problem (6) turns to

$$\min_{\mathbf{x}} \frac{1}{2} \|\mathbf{y} - \mathbf{S}\mathbf{H}\mathbf{x}\|_2^2 + \tau \|\mathbf{x} - \bar{\mathbf{x}}\|_2^2. \quad (14)$$

This implies that the target image \mathbf{x} is *a priori* close to the image $\bar{\mathbf{x}}$. The image $\bar{\mathbf{x}}$ can be an estimation of the HR image, e.g., an interpolated version of the observed image, a restored image obtained with learning-based algorithms [7] or a cleaner image obtained from other sensors [24], [35], [49]. In such case, using Theorem 1, the solution of the problem (14) is

$$\hat{\mathbf{x}} = \frac{1}{2\tau} \mathbf{r} - \frac{1}{2\tau} \mathbf{F}^H \underline{\mathbf{\Lambda}}^H (2\tau d \mathbf{I}_{N_l} + \underline{\mathbf{\Lambda}} \underline{\mathbf{\Lambda}}^H)^{-1} \underline{\mathbf{\Lambda}} \mathbf{F} \mathbf{r} \quad (15)$$

with $\mathbf{r} = \mathbf{H}^H \mathbf{S}^H \mathbf{y} + 2\tau \bar{\mathbf{x}}$.

Algorithm 1 summarizes the implementation of the proposed SR solution (15), which is referred to as *fast super-resolution (FSR)* approach.

C. Solution of the $\ell_2 - \ell_2$ problem in the gradient domain

Generic image priors defined in the gradient domain have been successfully used for image reconstruction, avoiding the common ringing artifacts see, e.g., [8], [9], [17]. In this part, we focus on the gradient profile prior proposed in [17] for the single image SR problem. This prior consists of considering the regularizing term $\|\nabla \mathbf{x} - \bar{\nabla} \mathbf{x}\|_2^2$, thus the problem (6) turns to

$$\min_{\mathbf{x}} \frac{1}{2} \|\mathbf{y} - \mathbf{S}\mathbf{H}\mathbf{x}\|_2^2 + \tau \|\nabla \mathbf{x} - \bar{\nabla} \mathbf{x}\|_2^2 \quad (16)$$

Algorithm 1: FSR with image-domain ℓ_2 -regularization: implementation of the analytical solution (15)

Input: \mathbf{y} , \mathbf{H} , \mathbf{S} , $\bar{\mathbf{x}}$, τ , d

// Factorization of \mathbf{H} (FFT of the blurring kernel)

1 $\mathbf{H} = \mathbf{F}^H \mathbf{\Lambda} \mathbf{F}$;

// Compute $\underline{\mathbf{\Lambda}}$

2 $\underline{\mathbf{\Lambda}} = [\mathbf{\Lambda}_1, \mathbf{\Lambda}_2, \dots, \mathbf{\Lambda}_d]$;

// Calculate FFT of \mathbf{r} denoted as \mathbf{Fr}

3 $\mathbf{Fr} = \mathbf{F}(\mathbf{H}^H \mathbf{S}^H \mathbf{y} + 2\tau \bar{\mathbf{x}})$;

// Hadamard (or entrywise) product in frequency domain

4 $\mathbf{x}_f = \left(\underline{\mathbf{\Lambda}}^H (2\tau d \mathbf{I}_{N_l} + \underline{\mathbf{\Lambda}} \underline{\mathbf{\Lambda}}^H)^{-1} \underline{\mathbf{\Lambda}} \right) \mathbf{Fr}$;

// Compute the analytical solution

5 $\hat{\mathbf{x}} = \frac{1}{2\tau} (\mathbf{r} - \mathbf{F}^H \mathbf{x}_f)$;

Output: $\hat{\mathbf{x}}$

where ∇ is the discrete version of the gradient $\nabla := [\partial_h, \partial_v]^T$ and $\bar{\nabla} \mathbf{x}$ is the estimated gradient field. More explanations about the motivations for using the gradient field may be found in [8], [17]. For an image $\mathbf{x} \in \mathbb{R}^{m \times n}$, under the periodic boundary conditions, the numerical definitions of the gradient operators are

$$\begin{aligned} (\partial_h \mathbf{x})(i, j) &= \mathbf{x}((i+1) \bmod m, j) - \mathbf{x}(i, j) && \text{if } i \leq m \\ (\partial_v \mathbf{x})(i, j) &= \mathbf{x}(i, (j+1) \bmod n) - \mathbf{x}(i, j) && \text{if } j \leq n \end{aligned}$$

where ∂_h and ∂_v are the horizontal and vertical gradients. The gradient operators can be rewritten as two BCCB matrices \mathbf{D}_h and \mathbf{D}_v corresponding to the horizontal and vertical discrete differences of an image, respectively. Therefore, two diagonal matrices $\mathbf{\Sigma}_h$ and $\mathbf{\Sigma}_v$ ($\mathbb{C}^{N_h \times N_h}$) are obtained by decomposing \mathbf{D}_h and \mathbf{D}_v in the frequency domain, i.e.,

$$\mathbf{D}_h = \mathbf{F}^H \mathbf{\Sigma}_h \mathbf{F} \text{ and } \mathbf{D}_v = \mathbf{F}^H \mathbf{\Sigma}_v \mathbf{F}. \quad (17)$$

Thus, the problem (16) can be transformed into

$$\min_{\mathbf{x}} \frac{1}{2} \|\mathbf{y} - \mathbf{S} \mathbf{H} \mathbf{x}\|_2^2 + \tau \|\mathbf{A} \mathbf{x} - \mathbf{v}\|_2^2 \quad (18)$$

with $\mathbf{A} = [\mathbf{D}_h^T, \mathbf{D}_v^T] \in \mathbb{R}^{2N_h \times N_h}$ and using the notation $\bar{\nabla} \mathbf{x} = \mathbf{v} = [\mathbf{v}_h, \mathbf{v}_v]^T \in \mathbb{R}^{2N_h \times 1}$. Note that the invertibility of $\mathbf{A}^H \mathbf{A}$ is violated here because of the periodic boundary assumption.

Thus, adding a small ℓ_2 -norm regularization $\tau\sigma\|\mathbf{x}\|_2^2$ (where σ is a very small constant) to (18) can circumvent this invertibility problem while keeping the solution close to the original regularization. Using Theorem 1, the analytical solution of (18) (including the additional small ℓ_2 -norm term) is given by (13) with $\Psi = (\Sigma_h^H \Sigma_h + \Sigma_v^H \Sigma_v + \sigma \mathbf{I}_{N_h})^{-1}$.

The pseudocode used to implement this solution is summarized in Algo. 2.

Algorithm 2: FSR with gradient-domain ℓ_2 -regularization: implementation of the analytical solution of (16)

Input: \mathbf{y} , \mathbf{H} , \mathbf{S} , \mathbf{D}_h , \mathbf{D}_v , $\bar{\nabla}\mathbf{x}$, τ , d

// Factorizations of matrices \mathbf{H} , \mathbf{D}_h , \mathbf{D}_v

- 1 $\mathbf{H} = \mathbf{F}^H \mathbf{\Lambda} \mathbf{F}$;
- 2 $\mathbf{D}_h = \mathbf{F}^H \Sigma_h \mathbf{F}$;
- 3 $\mathbf{D}_v = \mathbf{F}^H \Sigma_v \mathbf{F}$;

// Compute $\underline{\mathbf{\Lambda}}$ and Ψ

- 4 $\underline{\mathbf{\Lambda}} = [\mathbf{\Lambda}_1, \mathbf{\Lambda}_2, \dots, \mathbf{\Lambda}_d]$;
- 5 $\Psi = (\Sigma_h^H \Sigma_h + \Sigma_v^H \Sigma_v + \sigma \mathbf{I}_{N_h})^{-1}$;

// Calculate FFT of \mathbf{r} denoted as \mathbf{Fr}

- 6 $\mathbf{Fr} = \mathbf{F}(\mathbf{H}^H \mathbf{S}^H \mathbf{y} + 2\tau \mathbf{D}^H \mathbf{v})$;

// Hadamard (or entrywise) product in the frequency domain

- 7 $\mathbf{x}_f = \left[\Psi \underline{\mathbf{\Lambda}}^H (\mu d \mathbf{I}_{N_l} + \underline{\mathbf{\Lambda}} \Psi \underline{\mathbf{\Lambda}}^H)^{-1} \underline{\mathbf{\Lambda}} \Psi \right] \mathbf{Fr}$;

// Compute the analytical solution

- 8 $\hat{\mathbf{x}} = \frac{1}{2\tau} (\mathbf{F}^H \Psi \mathbf{Fr} - \mathbf{F}^H \mathbf{x}_f)$;

Output: $\hat{\mathbf{x}}$

IV. GENERALIZED FAST SUPER-RESOLUTION

As mentioned previously, a large variety of non-Gaussian regularizations has been proposed for the single image SR problem, in both image or transformed domains. Many SR algorithms, e.g., [5], [18], require to solve an $\ell_2 - \ell_2$ problem similar to (6) as an intermediate step. This section shows that the solution (13) derived in Section III can be combined with existing SR iterative methods to significantly lighten their computational costs.

A. General form of the proposed algorithm

In order to use the analytical solution (13) derived for the ℓ_2 -regularized SR problem into an ADMM framework, the problem (4) is rewritten as the following constrained optimization

problem

$$\begin{aligned} \min_{\mathbf{x}, \mathbf{u}} \quad & \frac{1}{2} \|\mathbf{y} - \mathbf{S}\mathbf{H}\mathbf{x}\|_2^2 + \tau\phi(\mathbf{u}) \\ \text{subject to} \quad & \mathbf{A}\mathbf{x} = \mathbf{u}. \end{aligned} \quad (19)$$

The AL function associated with this problem is

$$\begin{aligned} \mathcal{L}(\mathbf{x}, \mathbf{u}, \boldsymbol{\lambda}) = \\ \frac{1}{2} \|\mathbf{y} - \mathbf{S}\mathbf{H}\mathbf{u}\|_2^2 + \tau\phi(\mathbf{u}) + \boldsymbol{\lambda}^T (\mathbf{A}\mathbf{x} - \mathbf{u}) + \frac{\mu}{2} \|\mathbf{A}\mathbf{x} - \mathbf{u}\|_2^2 \end{aligned}$$

or equivalently

$$\mathcal{L}(\mathbf{x}, \mathbf{u}, \mathbf{d}) = \frac{1}{2} \|\mathbf{y} - \mathbf{S}\mathbf{H}\mathbf{u}\|_2^2 + \tau\phi(\mathbf{u}) + \frac{\mu}{2} \|\mathbf{A}\mathbf{x} - \mathbf{u} + \mathbf{d}\|_2^2. \quad (20)$$

To solve problem (19), we need to minimize $\mathcal{L}(\mathbf{x}, \mathbf{u}, \mathbf{d})$ w.r.t. \mathbf{x} and \mathbf{u} and update the scaled dual variable \mathbf{d} iteratively as summarized in Algo. 3.

Note that the 3rd step updating the HR image \mathbf{x} can be solved analytically using Theorem 1. The variable \mathbf{u} is updated at the 4th step using the Moreau proximity operator whose definition is given by

$$\text{prox}_{\lambda, \phi}(\boldsymbol{\nu}) = \underset{\mathbf{x}}{\text{argmin}} \phi(\mathbf{x}) + \frac{1}{2\lambda} \|\mathbf{x} - \boldsymbol{\nu}\|^2. \quad (21)$$

The generic optimization scheme given in Algo. 3, including the non-iterative update of the HR image following Theorem 1, is detailed hereafter for three widely used regularization techniques, namely for the TV regularization [18], the ℓ_1 -norm regularization in the wavelet domain [39] and the learning-based method in [7].

Algorithm 3: Proposed generalized fast super-resolution (FSR) scheme

Input: \mathbf{y} , \mathbf{S} , \mathbf{H} , d , τ ;

1 Set $k = 0$, choose $\mu > 0$, \mathbf{u}^0 , \mathbf{d}^0 ;

2 **Repeat**

3 $\mathbf{x}^{k+1} = \underset{\mathbf{x}}{\text{argmin}} \|\mathbf{y} - \mathbf{S}\mathbf{H}\mathbf{x}\|_2^2 + \mu \|\mathbf{A}\mathbf{x} - \mathbf{u}^k + \mathbf{d}^k\|_2^2$;

4 $\mathbf{u}^{k+1} = \underset{\mathbf{u}}{\text{argmin}} \tau\phi(\mathbf{u}) + \frac{\mu}{2} \|\mathbf{A}\mathbf{x}^{k+1} - \mathbf{u} + \mathbf{d}^k\|_2^2$;

5 $\mathbf{d}^{k+1} = \mathbf{d}^k + (\mathbf{A}\mathbf{x}^{k+1} - \mathbf{u}^{k+1})$;

6 **until** stopping criterion is satisfied.

B. TV regularization

Using a TV prior, problem (4) can be rewritten as

$$\min_{\mathbf{x}} \frac{1}{2} \|\mathbf{y} - \mathbf{S}\mathbf{H}\mathbf{x}\|_2^2 + \tau \phi(\mathbf{A}\mathbf{x}) \quad (22)$$

where the regularization term is given by

$$\phi(\mathbf{A}\mathbf{x}) = \|\mathbf{x}\|_{\text{TV}} = \sqrt{\|\mathbf{D}_h\mathbf{x}\|^2 + \|\mathbf{D}_v\mathbf{x}\|^2} \quad (23)$$

with $\mathbf{A} = [\mathbf{D}_h, \mathbf{D}_v]^T \in \mathbb{R}^{2N_h \times N_h}$. We can solve (22) using Algo. 3, with the auxiliary variable $\mathbf{u} = [\mathbf{u}_h, \mathbf{u}_v]^T \in \mathbb{R}^{2N_h \times 1}$ such that $\mathbf{A}\mathbf{x} = \mathbf{u}$. The resulting pseudocodes of the proposed fast SR approach for solving (22) are detailed in Algo. 4, which is reported in Appendix B.

C. ℓ_1 -norm regularization in the wavelet domain

Assuming that \mathbf{x} can be decomposed as a linear combination of wavelets (e.g., as in [37]), the SR can be conducted in the wavelet domain. Denote as $\mathbf{x} = \mathbf{W}\boldsymbol{\theta}$ the wavelet decomposition of \mathbf{x} , where $\boldsymbol{\theta} \in \mathbb{R}^{N_h \times 1}$ is the vector containing the wavelet coefficients and multiplying by the matrices \mathbf{W}^H and \mathbf{W} ($\in \mathbb{R}^{N_h \times N_h}$) represent the wavelet and inverse wavelet transforms (satisfying that $\mathbf{W}\mathbf{W}^H = \mathbf{W}^H\mathbf{W} = \mathbf{I}_{N_h}$). The single image SR with ℓ_1 -norm regularization in the wavelet domain can be formulated as follows

$$\min_{\mathbf{x}} \frac{1}{2} \|\mathbf{y} - \mathbf{S}\mathbf{H}\mathbf{x}\|_2^2 + \tau \|\mathbf{A}\mathbf{x}\|_1 \quad (24)$$

where $\mathbf{A} = \mathbf{W}^H$. By introducing the additional variable $\mathbf{u} = \mathbf{W}^H\mathbf{x}$, the problem (24) can be solved using Algo. 3. The corresponding pseudocodes of the resulting fast SR algorithm with an ℓ_1 -norm regularization in the wavelet domain are detailed in Algo. 5 in Appendix B.

D. Learning-based ℓ_2 -norm regularization

The effectiveness of the learning-based regularization for image reconstruction has been proved in several studies. In particular, Yang *et al.* [7] solved the single image SR problem by jointly training two dictionaries for the LR and HR image patches and by applying sparse coding (SC). Interestingly, the HR image \mathbf{x}_0 obtained by sparse coding was projected onto

the solution space satisfying (1), leading to the following optimization problem

$$\hat{\mathbf{x}} = \underset{\mathbf{x}}{\operatorname{argmin}} \frac{1}{2} \|\mathbf{y} - \mathbf{S}\mathbf{H}\mathbf{x}\|_2^2 + \tau \|\mathbf{x} - \mathbf{x}_0\|_2^2. \quad (25)$$

This optimization problem was solved using a gradient descent approach in [7]. However, it can benefit from the analytical solution provided by Theorem 1 that can be implemented using Algo. 1.

V. EXPERIMENTAL RESULTS

This section demonstrates the efficiency of the proposed fast SR strategy by testing it on various images with different regularization terms. The performance of the single image SR algorithms is evaluated in terms of reconstruction quality and computational load. Given the ability of our algorithm to solve the SR problem with less complexity than the existing methods, one may expect a gain in computational time and convergence properties. All the experiments were performed using MATLAB 2013A on a computer with Windows 7, Intel(R) Core(TM) i7-4770 CPU @3.40GHz and 8 GB RAM¹. Color images were processed using the illuminate channel only, as in [7]. Precisely, the RGB images were transformed into YUV coordinates and the color channels (Cb,Cr) were up-sampled using bicubic interpolation. In the illuminate channel, the HR image was blurred and down-sampled in each spatial direction with factors d_r and d_c . The resulting blurred and decimated images were then contaminated by AWGN of variance σ_n^2 with a blurred-signal-to-noise ratio defined by

$$\text{BSNR} = 10 \log_{10} \left(\frac{\|\mathbf{S}\mathbf{H}\mathbf{x} - E(\mathbf{S}\mathbf{H}\mathbf{x})\|_2^2}{N\sigma_n^2} \right) \quad (26)$$

where N is the total number of pixels of the observed image and $E(\cdot)$ is the arithmetic mean operator.

Unless explicitly specified, the blurring kernel is a 2D-Gaussian filter of size 9×9 with variance $\sigma_h^2 = 3$, the decimation factors are $d_r = d_c = 4$ and the noise level is $\text{BSNR} = 30\text{dB}$.

The performances of the different SR algorithms are evaluated both visually and quantitatively in terms of the following metrics: root mean square error (RMSE), peak signal-to-noise

¹The MATLAB codes are available in the first author's homepage <http://zhao.perso.enseeiht.fr/>

ratio (PSNR), improved signal-to-noise ratio (ISNR) and mean structural similarity (MSSIM). The definitions of these metrics, widely used to evaluate image reconstruction methods, are given below

$$\text{RMSE} = \sqrt{\|\mathbf{x} - \hat{\mathbf{x}}\|^2} \quad (27)$$

$$\text{PSNR} = 20 \log_{10} \frac{\max(\mathbf{x}, \hat{\mathbf{x}})}{\text{RMSE}} \quad (28)$$

$$\text{ISNR} = 10 \log_{10} \frac{\|\mathbf{x} - \bar{\mathbf{y}}\|^2}{\|\mathbf{x} - \hat{\mathbf{x}}\|^2} \quad (29)$$

$$\text{MSSIM} = \frac{1}{M} \sum_{j=1}^M \text{SSIM}(\mathbf{x}_j, \hat{\mathbf{x}}_j) \quad (30)$$

where the vectors $\mathbf{x}, \bar{\mathbf{y}}, \hat{\mathbf{x}}$ are the ground truth (reference image/HR image), the bicubic interpolated image and the restored SR image respectively and $\max(\mathbf{x}, \hat{\mathbf{x}})$ defines the largest value of \mathbf{x} and $\hat{\mathbf{x}}$. Note that MSSIM is implemented blockwise, with M the number of local windows, \mathbf{x}_j and $\hat{\mathbf{x}}_j$ are local regions extracted from \mathbf{x} and $\hat{\mathbf{x}}$ and SSIM is the structural similarity measure of each window (defined in [50]). Note that it is nonsensical to compute the ISNR for bicubic interpolation (always be 0) due to its definition.

A. Fast SR using ℓ_2 -regularizations

1) $\ell_2 - \ell_2$ model in the image domain:

a) *Gaussian blurring kernel:* We first explore the single image SR problem with the ‘‘pepper’’ image and standard Tikhonov/Gaussian regularization corresponding to the optimization problem formulated in (14). The size of the ground truth HR image shown in Fig. 2(b) is 512×512 . Fig. 2(c)–2(f) show the restored images with bicubic interpolation, the proposed analytical solution given in Algo. 1 and the splitting algorithm ADMM of [18] adapted to a Gaussian prior. The prior mean image $\bar{\mathbf{x}}$ (approximated HR image) is the up-sampled version of the LR image by bicubic interpolation (Case 1) with the results in Fig. 2(e) and 2(d), whereas $\bar{\mathbf{x}}$ is the ground truth (Case 2) with the results in Fig. 2(g) and 2(f). The regularization parameter was $\tau = 1$ in Case 1 and $\tau = 0.1$ in Case 2. The numerical results corresponding to this experiment are summarized in Table I. The visual impression

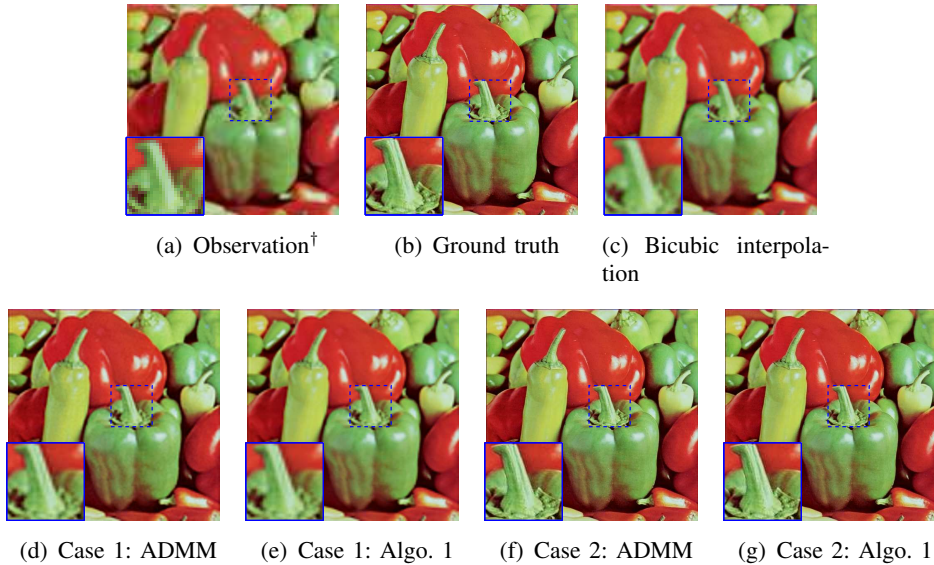


Fig. 2. SR of the pepper image when considering an $\ell_2 - \ell_2$ -model in the image domain: visual results. The prior image mean \bar{x} is defined as the bicubic interpolated LR image in Case 1 and as the ground truth HR image in Case 2.

†Note that the LR images have been scaled for better visualization in this figure (i.e., the actual LR images contain d times fewer pixels than the corresponding HR images).

and the numerical results show that the reconstructed HR images obtained with our method are similar to those obtained with ADMM. However, the proposed FSR method performs much faster than ADMM. More precisely, the computational time with our method is divided by a factor of 60 for Case 1 and by a factor of 80 for Case 2. Note also that the restored images obtained with Case 2 (\bar{x} set to the ground truth) are visually much better than the ones obtained with Case 1 (\bar{x} equal to the interpolated LR image), as expected.

TABLE I
SR OF THE PEPPER IMAGE WHEN CONSIDERING AN $\ell_2 - \ell_2$ -MODEL IN THE IMAGE DOMAIN: QUANTITATIVE RESULTS.

Method	PSNR (dB)	ISNR (dB)	MSSIM	Time (s.)
Bicubic	25.37	-	0.59	0.002
Case 1				
ADMM	29.26	4.01	0.67	1.92
Algo. 1	29.27	4.01	0.67	0.02
Case 2				
ADMM	53.84	29.27	1	0.5
Algo. 1	53.74	29.55	1	0.02

The performance of the proposed method has been also evaluated with various experimental parameters, namely, the BSNR level, the size of the blurring kernel and the decimation factors.

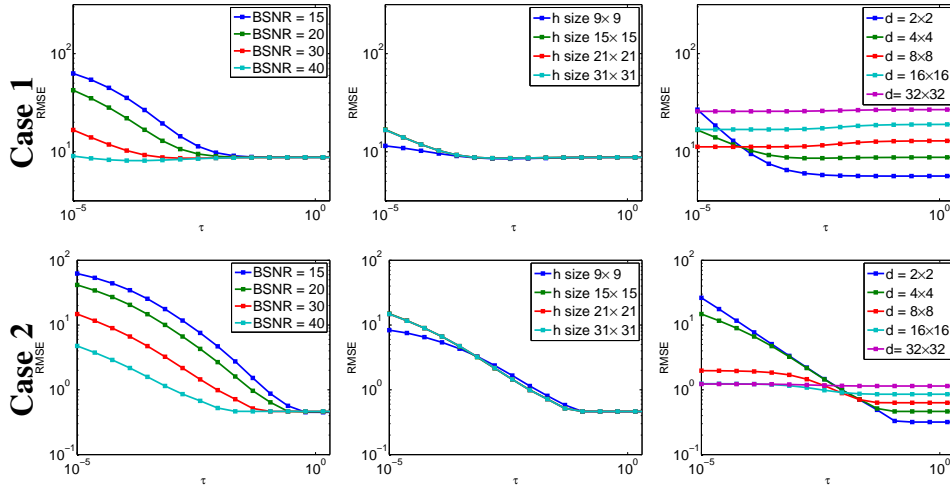


Fig. 3. SR of the “pepper” image when considering the $\ell_2 - \ell_2$ model in the image domain: RMSE as functions of the regularization parameter τ for various noise levels (1st column), blurring kernel sizes (2nd column) and decimation factors (3rd column). The results in the 1st column were obtained for $d_r = d_c = 4$ and 9×9 kernel size; in the 2nd column, $d_r = d_c = 4$ and BSNR= 30 dB; in the 3rd column, the kernel size was 9×9 and BSNR= 30 dB.

The corresponding RMSEs are depicted in Fig. 3 as functions of the regularization parameter τ for the two considered scenarios (Cases 1 and 2). Note that the same performance is obtained by the ADMM-based SR technique since it solves the same optimization problem.

b) Motion blurring kernel: This paragraph considers a dataset composed of images that have been captured by a camera placed on a tripod, whose Z-axis rotation handle has been locked and X- and Y-axis rotation handles have been loosen [51]. The corresponding dataset is available online². The observed LR image, motion kernel and corresponding SR results are shown in Fig. 4. The size of the motion kernel is 19×19 . As in the previous paragraph, the prior mean image \bar{x} is the bicubic interpolation of the LR image in Case 1, while \bar{x} is the ground truth in Case 2. The regularization parameter is set to $\tau = 0.01$ and $\tau = 0.1$ in Cases 1 and 2, respectively. Quantitative results are reported in Table II and show that the proposed method provides competitive results w.r.t. the other methods, while being more computational efficient.

2) $\ell_2 - \ell_2$ model in the gradient domain: This section compares the performance of the proposed fast SR strategy with the gradient profile regularization proposed in [8]. As shown in Section III-A, Theorem 1 allows the analytical SR solution to be computed. The “face”

²Available online at <http://www.wisdom.weizmann.ac.il/~levina/papers/LevinEtalCVPR09Data.zip>

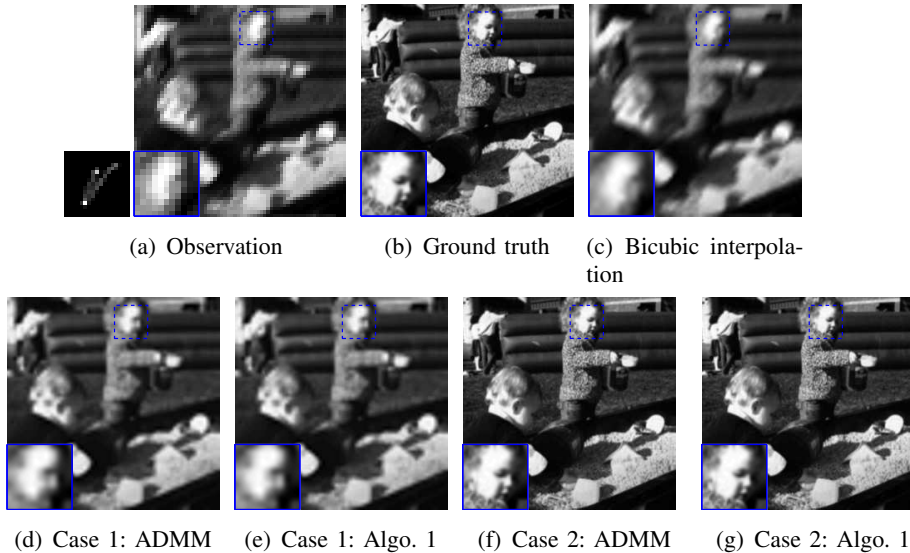


Fig. 4. SR of the motion blurred image when considering an $\ell_2 - \ell_2$ -model in the image domain: visual results. The prior image mean \bar{x} is defined as the bicubic interpolated LR image in Case 1 and as the ground truth HR image in Case 2.

TABLE II
SR OF THE MOTION BLURRED IMAGE WHEN CONSIDERING AN $\ell_2 - \ell_2$ -MODEL IN THE IMAGE DOMAIN: QUANTITATIVE RESULTS.

Method	PSNR (dB)	ISNR (dB)	MSSIM	Time (s.)
Bicubic	21.15	-	0.91	0.002
Case 1				
ADMM	27.11	5.96	0.96	0.11
Algo. 1	27.11	5.96	0.96	0.01
Case 2				
ADMM	53.23	32.08	1	0.42
Algo. 1	53.23	32.08	1	0.01

image (of size 276×276) shown in Fig. 5(b) was used for these tests. In this experiment, $\nabla \bar{x}$ is calculated using the reference HR image and the regularization parameters have been set to $\tau = 10^{-3}$ and $\sigma = 10^{-8}$. The proposed method is compared with the ADMM as well as the CG method instead of the gradient descent (GD) method initially proposed in [17] (since CG has shown to be much more efficient than GD in this experiment). The restored images using bicubic interpolation, ADMM, the CG method and the proposed Algo. 2 are shown in Fig. 5(c)-5(e). The corresponding numerical results are reported in Table III. These results illustrate the superiority of the approach in terms of computational time. This significant difference can be explained by the non-iterative nature of the proposed method compared

to CG and ADMM. Moreover, all the three methods converge to the same global minima as shown by the objective curves in Fig. 6. The convergence of the objective curves is in agreement with the visual and numerical results.

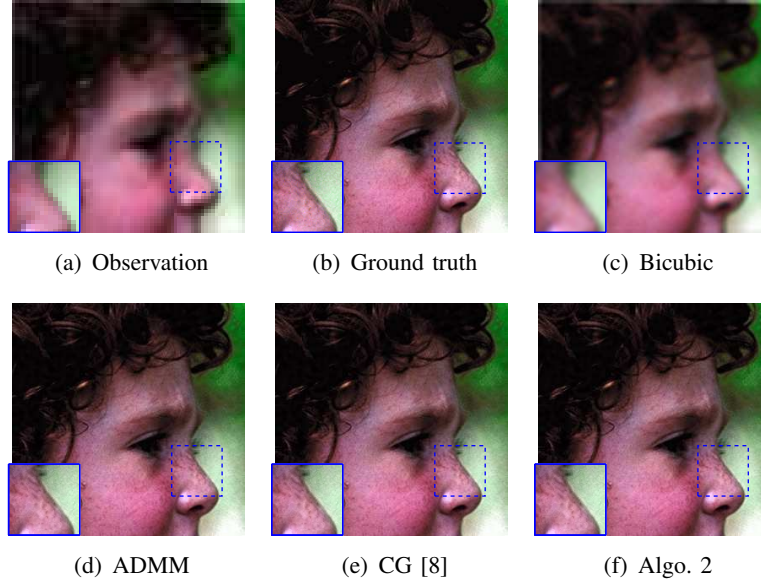


Fig. 5. SR of the face image when considering an $\ell_2 - \ell_2$ -model in the gradient domain: visual results.

TABLE III
SR OF THE FACE IMAGE WHEN CONSIDERING AN $\ell_2 - \ell_2$ -MODEL IN THE GRADIENT DOMAIN: QUANTITATIVE RESULTS.

Method	PSNR (dB)	ISNR (dB)	MSSIM	Time (s.)
Bicubic	26.84	-	0.49	0.001
ADMM	42.82	15.98	0.98	0.71
CG	42.82	15.98	0.98	0.35
Algo. 2	42.82	15.98	0.98	0.009

3) *Learning-based ℓ_2 -norm regularization*: This section studies the performance of the algorithm obtained when the analytical solution of Theorem 1 is embedded in the learning-based method of [7]. The method investigated in [7] computed an initial estimation of the HR image via sparse coding (SC) and used a back-projection (BP) procedure to improve the SR performance. The BP operation was performed by a GD method in [7]. Here, this GD step has been replaced by the analytical solution provided by Theorem 1 and Algo. 1. The image

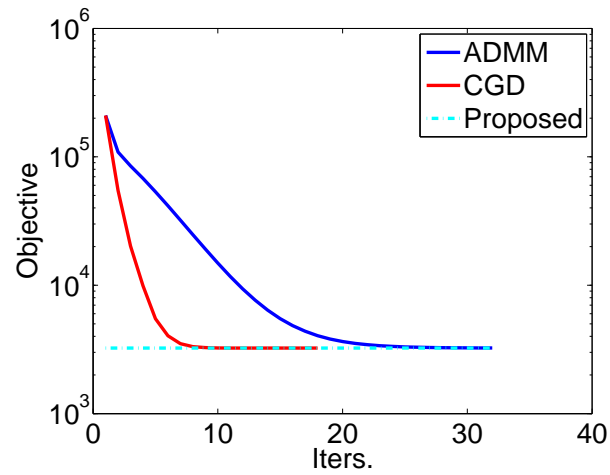


Fig. 6. SR of the face image when considering an $\ell_2 - \ell_2$ -model in the gradient domain: objective functions.

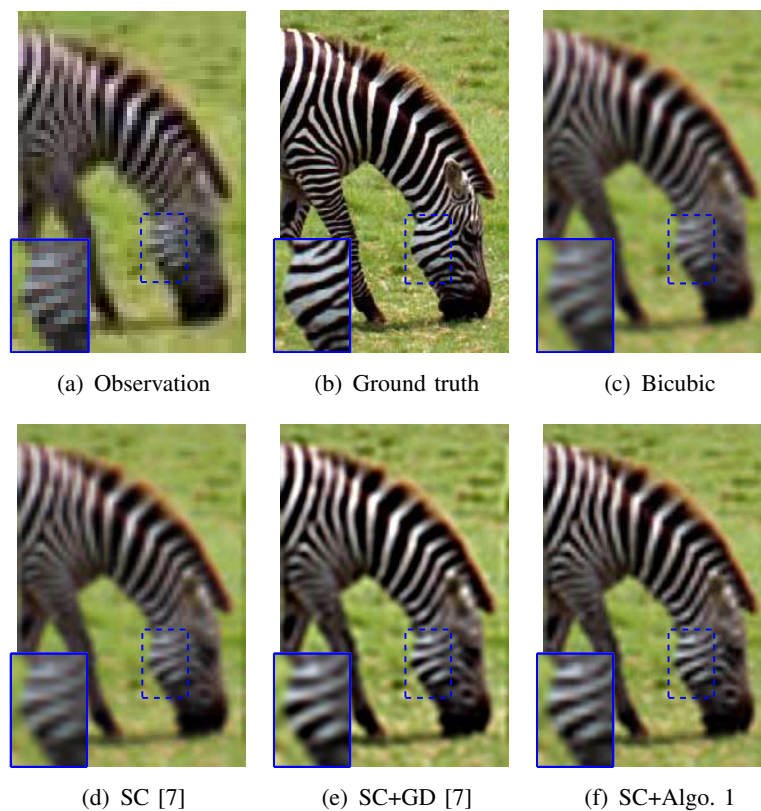


Fig. 7. SR of the zebra image when considering a learning-based ℓ_2 -norm regularization: visual results.

“zebra” was used in this experiment to compare the performance of both algorithms³. The

³For comparison purpose, the authors used the MATLAB code corresponding to [7] available at <http://www.ifp.illinois.edu/~jyang29>.

LR and HR images (of size 300×200) are shown in Fig. 7(a) and 7(b). The regularization parameter was set to $\tau = 0.1$. The restored images shown in Figs. 7(c)-7(e) were obtained using the initial SC estimation proposed in [7], the back-projected SC image combined with the gradient descent (GD) algorithm of [7] (referred to as “SC + GD”) and the proposed closed-form solution (referred to as “SC + Algo. 1”). The corresponding numerical results are reported in Table IV. The restored images obtained with the two back-projection approaches are clearly better than the restoration obtained with the SC method. While the quality of the images obtained with these projection approaches is similar, the use of the analytical solution of Theorem 1 allows the computational cost of the GD step to be reduced significantly.

TABLE IV
SR OF THE ZEBRA IMAGE WHEN CONSIDERING A LEARNING-BASED ℓ_2 -NORM REGULARIZATION: QUANTITATIVE RESULTS.

Method	PSNR (dB)	ISNR (dB)	MSSIM	Time (s.)
Bicubic	18.98	-	0.37	0.001
SC [7]	19.15	0.16	0.38	170.9
SC+GD [7]	20.76	1.78	0.47	170.9+1.23
SC+Algo. 1	29.99	1.88	0.48	170.9+ 0.01

B. Embedding the $\ell_2 - \ell_2$ analytical solution into the ADMM framework

In this second group of experiments, we consider two non-Gaussian priors that have been widely used for image reconstruction problems: the TV regularization in the spatial domain and the ℓ_1 -norm regularization in the wavelet domain. In both cases, the analytical solution of Theorem 1 is embedded into a standard ADMM algorithm inspired from [18] (the resulting algorithms referred to as Algo. 4 and 5 are detailed in Appendix C). The stopping criterion for both implementations is chosen as the relative cost function error defined as

$$\frac{|f(\mathbf{x}^{k+1}) - f(\mathbf{x}^k)|}{f(\mathbf{x}^k)} \quad (31)$$

where $f(\mathbf{x}) = \frac{1}{2}\|\mathbf{y} - \mathbf{S}\mathbf{H}\mathbf{x}\|_2^2 + \tau\phi(\mathbf{A}\mathbf{x})$. Note that other stopping criteria such as those studied in [52] could also be investigated. The 512×512 images “Lena”, “monarch” and “Barbara” were considered in these experiments. The observed LR images and the HR images (ground truth) are displayed in Fig. 8 (first two columns).

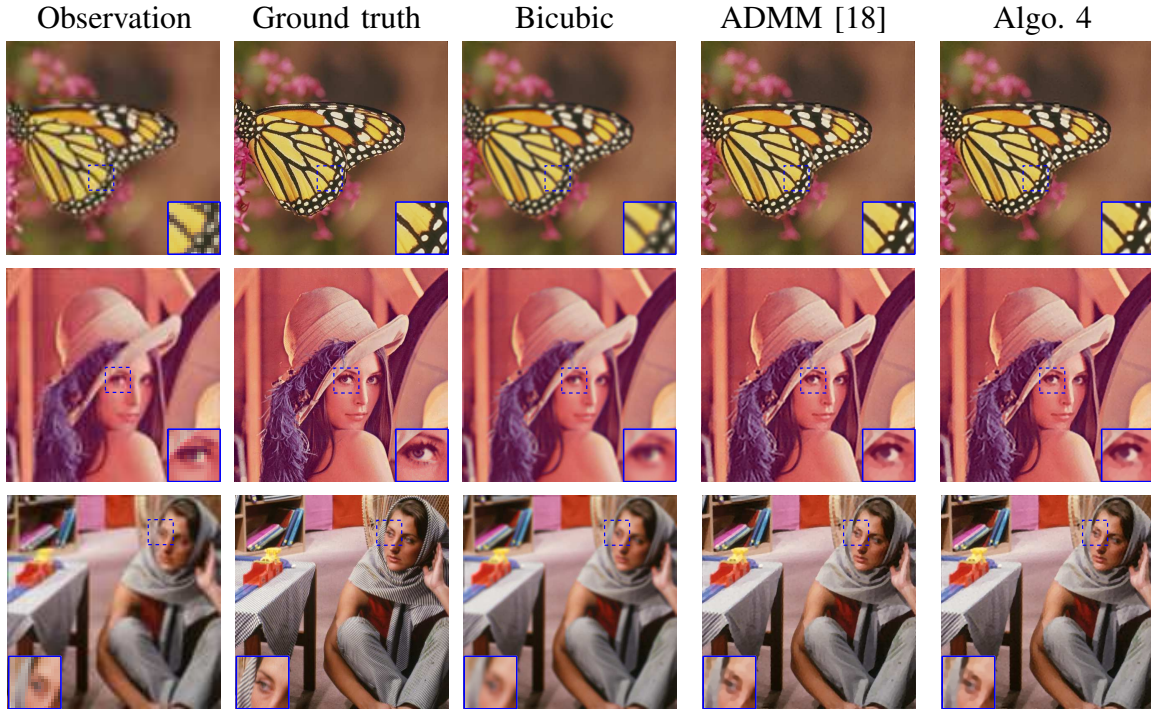


Fig. 8. SR of the Monarch, Lena and Barbara images when considering a TV-regularization: visual results.

1) *TV-regularization*: The regularization parameter was manually fixed (by cross validation) to $\tau = 2 \times 10^{-3}$ for the image “Lena”, to $\tau = 1.8 \times 10^{-3}$ for the image “monarch” and to $\tau = 2.5 \times 10^{-3}$ for the image “Barbara”. Fig. 8 shows the SR results obtained using the bicubic interpolation (third column), ADMM based algorithm of [18] (fourth column) and the proposed Algo. 4 (last column). As expected, the ADMM reconstructions perform much better than a simple interpolation of the LR image that is not able to solve the upsampling and deblurring problem. The results obtained with the proposed algorithm and with the method of [18] are visually very similar. This visual inspection is confirmed by the quantitative results provided in Table V. However, the proposed algorithm has the advantage of being much faster than the algorithm of [18] (with computational times reduced by a factor larger than 2). Moreover, Fig. 9 illustrates the convergence of the two algorithms. The proposed single image SR algorithm (Algo. 4) converges faster and with less fluctuations than the algorithm of [18]. This result can be explained by the fact that the algorithm in [18] requires to handle more variables in the ADMM scheme than the proposed algorithm.

TABLE V
SR OF THE MONARCH, LENA AND BARBARA IMAGES WHEN CONSIDERING A TV-REGULARIZATION: QUANTITATIVE RESULTS.

Image	Method	PSNR (dB)	ISNR (dB)	MSSIM	Time (s)	Iter.
Monarch	Bicubic	23.11	-	0.75	0.002	-
	ADMM [18]	29.49	6.38	0.84	78.95	812
	Algo. 4	29.38	6.28	0.83	19.81	170
Lena	Bicubic	25.80	-	0.57	0.002	-
	ADMM [18]	30.81	5.00	0.66	35.67	372
	Algo. 4	30.91	5.11	0.66	20.63	164
Barbara	Bicubic	22.71	-	0.48	0.002	-
	ADMM [18]	24.80	2.09	0.56	13.85	148
	Algo. 4	24.84	2.13	0.56	8.36	73

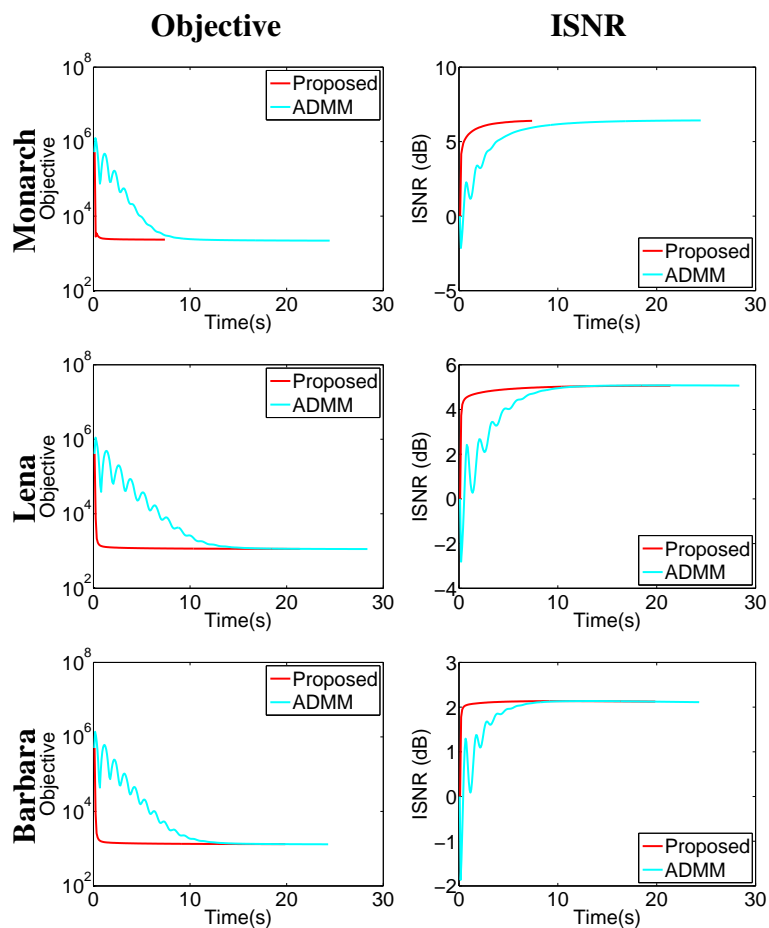


Fig. 9. SR of the Monarch, Lena and Barbara images when considering a TV-regularization: objective function (left) and ISNR (right) vs time.

2) ℓ_1 -norm regularization in the wavelet domain: This section evaluates the performance of Algo. 5, which is compared with a generalization of the method proposed in [18] to an ℓ_1 -norm regularization in the wavelet domain. The motivations for working in the wavelet domain are essentially to take advantage of the sparsity of the wavelet coefficients. All experiments were conducted using the discrete Haar wavelet transform and the Rice wavelet toolbox [53]. For both implementations, the regularization parameter was adjusted by cross validation, leading to $\tau = 2 \times 10^{-4}$ for the image “Lena”, $\tau = 1.8 \times 10^{-4}$ for the image “Monarch” and $\tau = 2.5 \times 10^{-4}$ for the image “Barbara”.

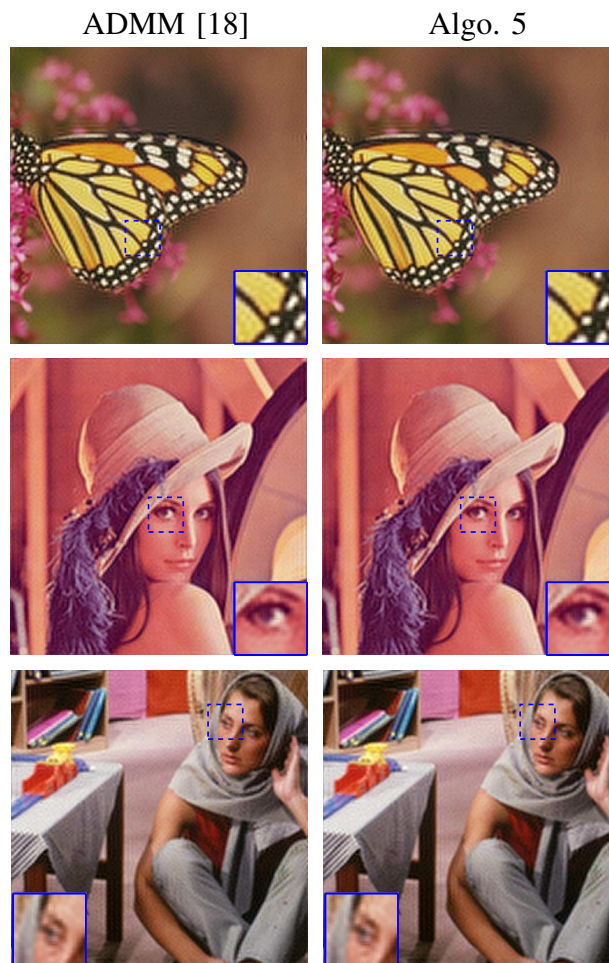


Fig. 10. SR of the Monarch, Lena and Barbara images when considering a ℓ_1 -norm regularization in the wavelet domain: visual results.

Fig. 10 shows the SR reconstruction results with an ℓ_1 -norm minimization in the wavelet domain. The HR images obtained with Algo. 5 and with the algorithm of [18] adapted to the ℓ_1 -norm prior are visually similar and better than a simple interpolation. The numerical

TABLE VI
SR OF THE MONARCH, LENA AND BARBARA IMAGES WHEN CONSIDERING A ℓ_1 -NORM REGULARIZATION IN THE WAVELET DOMAIN: QUANTITATIVE RESULTS.

Image	Method	PSNR (dB)	ISNR (dB)	MSSIM	Time (sec.)	Iter.
Monarch	Bicubic	23.11	-	0.75	0.002	-
	ADMM [18]*	27.08	3.97	0.74	34.08	400
	Algorithm 5	27.13	4.03	0.74	15.02	177
Lena	Bicubic	25.80	-	0.57	0.002	-
	ADMM [18]	30.09	4.29	0.62	38.48	450
	Algorithm 5	30.21	4.41	0.63	14.25	164
Barbara	Bicubic	22.71	-	0.48	0.002	-
	ADMM [18]	24.66	1.95	0.52	34.13	400
	Algorithm 5	24.70	2.00	0.53	14.83	171

*The algorithm of [18] was originally proposed for SR using a TV regularization. This algorithm has been modified by the authors to solve the ℓ_1 -norm penalized optimization problem.

results shown in Table VI confirm that the two algorithms provide similar reconstruction performance. However, as in the previous case (TV regularization), the proposed algorithm is characterized by much smaller computational times than the standard ADMM implementation. The faster and smoother convergence obtained with the proposed method (Algo. 5) can be observed in Fig. 11. Note that the fluctuations of the objective function and PSNR values (versus the number of iterations) obtained with the method of [18] are due to the variable splitting, which requires more variables and constraints to be handled than for the proposed method.

VI. CONCLUSION AND PERSPECTIVES

This paper studied a new fast single image super-resolution framework based on the widely used image formation model. The proposed super-resolution approach computed the super-resolved image efficiently by exploiting intrinsic properties of the decimation and the blurring operators in the frequency domain. A large variety of priors was shown to be able to be handled in the proposed super-resolution scheme. Specifically, when considering an ℓ_2 -regularization, the target image was computed analytically, getting rid of any iterative steps. For more complex priors (i.e., non ℓ_2 -regularization), variable splitting allowed this analytical solution to be embedded into the augmented Lagrangian framework, thus accelerating various existing schemes for single image super-resolution. Results on several natural images con-

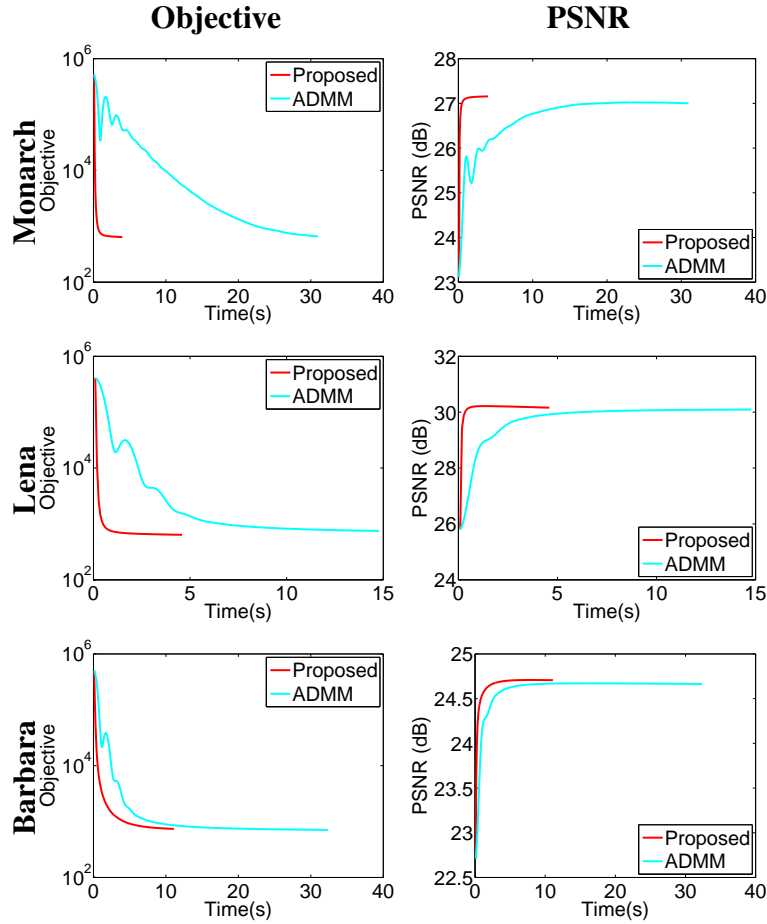


Fig. 11. SR of the Monarch, Lena and Barbara images when considering an ℓ_1 -norm regularization in the wavelet domain: objective function (left) and PSNR (right) vs time.

firmed the computational efficiency of the proposed approach and shown its fast and smooth convergence. As a perspective of this work, an interesting research track consists of extending the proposed method to some online applications such as video super-resolution and medical imaging, to evaluate its robustness to non-Gaussian noise and to extend it to semi-blind or blind deconvolution or multi-frame super-resolution. Considering a more practical case for super-resolving real images compressed by JPEG or JPEG-2000 algorithms will also be interesting and deserves further exploration.

APPENDIX A

DERIVATION OF THE ANALYTICAL SOLUTION (13)

The computational details for obtaining the result in (13) from (7) are summarized hereinafter. First, denoting $\mathbf{r} = \mathbf{H}^H \mathbf{S}^H \mathbf{y} + 2\tau \mathbf{A}^H \mathbf{v}$, the solution (7) is

$$\begin{aligned} \hat{\mathbf{x}} &= (\mathbf{H}^H \mathbf{S} \mathbf{H} + 2\tau \mathbf{A}^H \mathbf{A})^{-1} \mathbf{r} \\ &= \mathbf{F}^H (\mathbf{\Lambda}^H \mathbf{F} \mathbf{S} \mathbf{F}^H \mathbf{\Lambda} + 2\tau \mathbf{F} \mathbf{A}^H \mathbf{A} \mathbf{F}^H)^{-1} \mathbf{F} \mathbf{r}. \end{aligned} \quad (32)$$

Based on Lemma 1, $\mathbf{\Lambda}^H \mathbf{F} \mathbf{S} \mathbf{F}^H \mathbf{\Lambda}$ is computed as

$$\begin{aligned} &\mathbf{\Lambda}^H \mathbf{F} \mathbf{S} \mathbf{F}^H \mathbf{\Lambda} \\ &= \frac{1}{d} \mathbf{\Lambda}^H (\mathbf{J}_d \otimes \mathbf{I}_{N_l}) \mathbf{\Lambda} \end{aligned} \quad (33)$$

$$= \frac{1}{d} \mathbf{\Lambda}^H ((\mathbf{1}_d \mathbf{1}_d^T) \otimes (\mathbf{I}_{N_l} \mathbf{I}_{N_l})) \mathbf{\Lambda} \quad (34)$$

$$= \frac{1}{d} \mathbf{\Lambda}^H (\mathbf{1}_d \otimes \mathbf{I}_{N_l}) (\mathbf{1}_d^T \otimes \mathbf{I}_{N_l}) \mathbf{\Lambda} \quad (35)$$

$$= \frac{1}{d} \left(\mathbf{\Lambda}^H \underbrace{[\mathbf{I}_{N_l}, \dots, \mathbf{I}_{N_l}]^T}_d \right) \left(\underbrace{[\mathbf{I}_{N_l}, \dots, \mathbf{I}_{N_l}] \mathbf{\Lambda}}_d \right) \quad (36)$$

$$= \frac{1}{d} \underline{\mathbf{\Lambda}}^H \underline{\mathbf{\Lambda}}. \quad (37)$$

Note that (34) was obtained from (33) by replacing \mathbf{J}_d by $\mathbf{1}_d \mathbf{1}_d^T$, where $\mathbf{1}_d \in \mathbb{R}^{d \times 1}$ is a vector of ones. Obtaining (35) from (34) is straightforward using the following property of the Kronecker product \otimes

$$\mathbf{A} \mathbf{B} \otimes \mathbf{C} \mathbf{D} = (\mathbf{A} \otimes \mathbf{C})(\mathbf{B} \otimes \mathbf{D}).$$

In (36), $\mathbf{\Lambda} \in \mathbb{R}^{N_h \times N_h}$ whereas $[\mathbf{I}_{N_l}, \dots, \mathbf{I}_{N_l}] \in \mathbb{R}^{N_l \times N_h}$ and $[\mathbf{I}_{N_l}, \dots, \mathbf{I}_{N_l}]^T \in \mathbb{R}^{N_h \times N_l}$ are block matrices whose blocks are equal to the identity matrix \mathbf{I}_{N_l} . The matrix $\underline{\mathbf{\Lambda}} \in \mathbb{R}^{N_l \times N_h}$

in (37) is given by

$$\begin{aligned}
\mathbf{\underline{\Lambda}} &= [\mathbf{I}_{N_l}, \dots, \mathbf{I}_{N_l}] \mathbf{\Lambda} \\
&= [\mathbf{I}_{N_l}, \dots, \mathbf{I}_{N_l}] \text{diag}\{\mathbf{\Lambda}_1, \dots, \mathbf{\Lambda}_d\} \\
&= [\mathbf{I}_{N_l}, \dots, \mathbf{I}_{N_l}] \begin{bmatrix} \mathbf{\Lambda}_1 & \cdots & 0 \\ \vdots & \ddots & \vdots \\ 0 & \cdots & \mathbf{\Lambda}_d \end{bmatrix} \tag{38}
\end{aligned}$$

$$= [\mathbf{\Lambda}_1, \mathbf{\Lambda}_2, \dots, \mathbf{\Lambda}_d]. \tag{39}$$

As a consequence, (32) can be written as in (9), i.e.,

$$\hat{\mathbf{x}} = \mathbf{F}^H \left(\frac{1}{d} \mathbf{\underline{\Lambda}}^H \mathbf{\underline{\Lambda}} + 2\tau \mathbf{F} \mathbf{A}^H \mathbf{A} \mathbf{F}^H \right)^{-1} \mathbf{F} \mathbf{r} \tag{40}$$

$$= \mathbf{F}^H \left[\frac{1}{2\tau} \mathbf{\Psi} - \frac{1}{2\tau} \mathbf{\Psi} \mathbf{\underline{\Lambda}}^H \left(d \mathbf{I}_{N_l} + \frac{1}{2\tau} \mathbf{\underline{\Lambda}} \mathbf{\Psi} \mathbf{\underline{\Lambda}}^H \right)^{-1} \mathbf{\underline{\Lambda}} \mathbf{\Psi} \frac{1}{2\tau} \right] \mathbf{F} \mathbf{r} \tag{41}$$

$$= \frac{1}{2\tau} \mathbf{F}^H \mathbf{\Psi} \mathbf{F} \mathbf{r} - \frac{1}{2\tau} \mathbf{F}^H \mathbf{\Psi} \mathbf{\underline{\Lambda}}^H \left(2\tau d \mathbf{I}_{N_l} + \mathbf{\underline{\Lambda}} \mathbf{\Psi} \mathbf{\underline{\Lambda}}^H \right)^{-1} \mathbf{\underline{\Lambda}} \mathbf{\Psi} \mathbf{F} \mathbf{r} \tag{42}$$

where $\mathbf{\Psi} = \mathbf{F} (\mathbf{A}^H \mathbf{A})^{-1} \mathbf{F}^H$. The Lemma 2 is adopted from (40) to (41) with $\mathbf{A}_1 = 2\tau \mathbf{F} \mathbf{A}^H \mathbf{A} \mathbf{F}^H$, $\mathbf{A}_2 = \mathbf{\underline{\Lambda}}^H$, $\mathbf{A}_3 = \frac{1}{d} \mathbf{I}$ and $\mathbf{A}_4 = \mathbf{\underline{\Lambda}}$. Note that the matrices \mathbf{A}_1 and \mathbf{A}_3 are always invertible, implying that the Woodbury formula can be applied.

APPENDIX B

PSEUDO CODES OF THE PROPOSED FAST ADMM SUPER-RESOLUTION METHODS FOR TV AND ℓ_1 -NORM REGULARIZATIONS

Algorithm 4: FSR with TV regularization

Input: \mathbf{y} , \mathbf{H} , \mathbf{S} , τ , d , \mathbf{D}_h and \mathbf{D}_v
 1 Set $k = 0$, choose $\mu > 0$, \mathbf{d}^0 , \mathbf{u}^0 ;
 // Factorization of matrix \mathbf{H}
 2 $\mathbf{H} = \mathbf{F}^H \mathbf{\Lambda} \mathbf{F}$;
 3 $\underline{\mathbf{\Lambda}} = [\mathbf{\Lambda}_1, \mathbf{\Lambda}_2, \dots, \mathbf{\Lambda}_d]$;
 // Factorization of matrices \mathbf{D}_h and \mathbf{D}_v
 4 $\mathbf{D}_h = \mathbf{F}^H \mathbf{\Sigma}_h \mathbf{F}$;
 5 $\mathbf{D}_v = \mathbf{F}^H \mathbf{\Sigma}_v \mathbf{F}$;
 6 $\mathbf{\Psi} = (\mathbf{\Sigma}_h^H \mathbf{\Sigma}_h + \mathbf{\Sigma}_v^H \mathbf{\Sigma}_v)^{-1}$;
 7 **Repeat**
 // Update \mathbf{x} using Theorem 1
 8 $\boldsymbol{\rho}_h = \mathbf{u}_h^k - \mathbf{d}_h^k$;
 9 $\boldsymbol{\rho}_v = \mathbf{u}_v^k - \mathbf{d}_v^k$;
 10 $\mathbf{Fr} = \mathbf{F}(\mathbf{H}^H \mathbf{S}^H \mathbf{y} + \mu \mathbf{D}_h \boldsymbol{\rho}_h + \mu \mathbf{D}_v \boldsymbol{\rho}_v)$;
 11 $\mathbf{x}_f = \left(\mathbf{\Psi} \underline{\mathbf{\Lambda}}^H (\mu d \mathbf{I}_{N_l} + \underline{\mathbf{\Lambda}} \mathbf{\Psi} \underline{\mathbf{\Lambda}}^H)^{-1} \underline{\mathbf{\Lambda}} \mathbf{\Psi} \right) \mathbf{Fr}$;
 12 $\mathbf{x}^{k+1} = \frac{1}{\mu} \mathbf{F}^H \mathbf{\Psi} \mathbf{Fr} - \frac{1}{\mu} \mathbf{F}^H \mathbf{x}_f$;
 // Update \mathbf{u} using the vector-soft-thresholding operator
 13 $\boldsymbol{\nu} = [\mathbf{D}_h \mathbf{x}^{k+1} + \mathbf{d}_h^k, \mathbf{D}_v \mathbf{x}^{k+1} + \mathbf{d}_v^k]$;
 14 $\mathbf{u}^{k+1}[i] = \max\{\mathbf{0}, \|\boldsymbol{\nu}[i]\|_2 - \tau/\mu\} \frac{\boldsymbol{\nu}[i]}{\|\boldsymbol{\nu}[i]\|_2}$;
 // Update the dual variables \mathbf{d}
 15 $\mathbf{d}^{k+1} = \mathbf{d}^k + (\mathbf{A} \mathbf{x}^{k+1} - \mathbf{u}^{k+1})$;
 16 $k = k + 1$;
 17 until stopping criterion is satisfied;
Output: $\hat{\mathbf{x}} = \mathbf{x}^k$.

REFERENCES

- [1] S. C. Park, M. K. Park, and M. G. Kang, "Super-resolution image reconstruction: a technical overview," *IEEE Signal Process. Mag.*, vol. 20, pp. 21–36, 2003.
- [2] G. Martin and J. M. Bioucas-Dias, "Hyperspectral compressive acquisition in the spatial domain via blind factorization," in *Proc. IEEE Workshop on Hyperspectral Image and Signal Processing: Evolution in Remote Sensing (WHISPERS)*, Tokyo, Japan, June 2015.
- [3] J. Yang and T. Huang, *Super-resolution imaging*. Boca Raton, FL, USA: CRC Press, 2010, ch. Image super-resolution: Historical overview and future challenges, pp. 20–34.
- [4] T. Akgun, Y. Altunbasak, and R. M. Mersereau, "Super-resolution reconstruction of hyperspectral images," *IEEE Trans. Image Process.*, vol. 14, no. 11, pp. 1860–1875, 2005.
- [5] I. Yanovsky, B. H. Lambrigtsen, A. B. Tanner, and L. A. Vese, "Efficient deconvolution and super-resolution methods in microwave imagery," *IEEE J. Sel. Topics Appl. Earth Observations and Remote Sens.*, vol. 8, no. 9, pp. 4273–4283, 2015.
- [6] R. Morin, A. Basarab, and D. Kouame, "Alternating direction method of multipliers framework for super-resolution in

Algorithm 5: FSR with ℓ_1 -norm regularization in the wavelet domain

Input: \mathbf{y} , \mathbf{H} , \mathbf{S} , τ , d
1 Set $k = 0$, choose $\mu > 0$, \mathbf{d}^0 , \mathbf{u}^0 ;
 // Factorization of matrix \mathbf{H}
2 $\mathbf{H} = \mathbf{F}^H \mathbf{\Lambda} \mathbf{F}$;
3 $\underline{\mathbf{\Lambda}} = [\mathbf{\Lambda}_1, \mathbf{\Lambda}_2, \dots, \mathbf{\Lambda}_d]$;
4 Repeat
 // Update $\boldsymbol{\theta}$ using Theorem 1
5 $\mathbf{F} \mathbf{r} = \mathbf{F}(\mathbf{H}^H \mathbf{S}^H \mathbf{y} + \mu \mathbf{W}(\mathbf{u}^k - \mathbf{d}^k))$;
6 $\mathbf{x}_f = \left(\underline{\mathbf{\Lambda}}^H (\mu d \mathbf{I}_{N_l} + \underline{\mathbf{\Lambda}} \underline{\mathbf{\Lambda}}^H)^{-1} \underline{\mathbf{\Lambda}} \right) \mathbf{F} \mathbf{r}$;
7 $\mathbf{x}^{k+1} = \frac{1}{\mu} \mathbf{F} \mathbf{r} - \frac{1}{\mu} \mathbf{x}_f$;
 // Update \mathbf{u} using the soft-thresholding operator
8 $\boldsymbol{\nu} = \mathbf{W}^H \mathbf{x}^{k+1} + \mathbf{d}^k$;
9 $\mathbf{u}^{k+1} = \max\{0, |\boldsymbol{\nu}| - \tau/\mu\}$; // $|\boldsymbol{\nu}| \triangleq [|\nu_1|, \dots, |\nu_M|]^T \in \mathbb{R}^{M \times 1}$
 // Update the dual variables \mathbf{d}
10 $\mathbf{d}^{k+1} = \mathbf{d}^k + (\mathbf{W}^H \mathbf{x}^{k+1} - \mathbf{u}^{k+1})$;
11 $k = k + 1$;
12 until stopping criterion is satisfied;
Output: $\hat{\mathbf{x}} = \mathbf{x}^k$.

ultrasound imaging,” in *Proc. IEEE International Symposium on Biomedical Imaging (ISBI)*, Barcelona, Spain, May 2012, pp. 1595–1598.

- [7] J. Yang, J. Wright, T. S. Huang, and Y. Ma, “Image super-resolution via sparse representation,” *IEEE Trans. Image Process.*, vol. 19, no. 11, pp. 2861–2873, 2010.
- [8] J. Sun, J. Sun, Z. Xu, and H.-Y. Shum, “Image super-resolution using gradient profile prior,” in *Proc. IEEE Conference on Computer Vision and Pattern Recognition (CVPR)*, Anchorage, AK, 2008, pp. 1–8.
- [9] Y.-W. Tai, S. Liu, M. S. Brown, and S. Lin, “Super resolution using edge prior and single image detail synthesis,” in *Proc. IEEE Conference on Computer Vision and Pattern Recognition (CVPR)*, San Francisco, 2010, pp. 2400 – 2407.
- [10] P. Thévenaz, T. Blu, and M. Unser, in *Handbook of Medical Imaging*, I. N. Bankman, Ed. Orlando, FL, USA: Academic Press, Inc., 2000, ch. Image Interpolation and Resampling, pp. 393–420.
- [11] X. Zhang and X. Wu, “Image interpolation by adaptive 2-D autoregressive modeling and soft-decision estimation,” *IEEE Trans. Image Process.*, vol. 17, no. 6, pp. 887–896, 2008.
- [12] S. Mallat and G. Yu, “Super-resolution with sparse mixing estimators,” *IEEE Trans. Image Process.*, vol. 19, no. 11, pp. 2889–2900, 2010.
- [13] W. T. Freeman, E. C. Pasztor, and O. T. Carmichael, “Learning low-level vision,” *Int. J. Comput. Vision*, vol. 40, no. 1, pp. 25–47, Oct. 2000.
- [14] D. Glasner, S. Bagon, and M. Irani, “Super-resolution from a single image,” in *Proc. IEEE Int. Conf. Comp. Vision (ICCV)*, Kyoto, Japan, 2009, pp. 349 – 356.
- [15] J.-B. Huang, A. Singh, and N. Ahuja, “Single image super-resolution from transformed self-exemplars,” in *Proc. IEEE Conference on Computer Vision and Pattern Recognition (CVPR)*, Boston, Massachusetts, USA, 2015.
- [16] R. Zeyde, M. Elad, and M. Protter, “On single image scale-up using sparse-representations,” in *Curves and Surfaces*,

- ser. Lecture Notes in Computer Science, J.-D. Boissonnat, P. Chenin, A. Cohen, C. Gout, T. Lyche, M.-L. Mazure, and L. Schumaker, Eds. Springer Berlin Heidelberg, 2012, vol. 6920, pp. 711–730.
- [17] J. Sun, J. Sun, Z. Xu, and H.-Y. Shum, “Gradient profile prior and its applications in image super-resolution and enhancement,” *IEEE Trans. Image Process.*, vol. 20, no. 6, pp. 1529 – 1542, 2011.
- [18] M. K. Ng, P. Weiss, and X. Yuan, “Solving constrained total-variation image restoration and reconstruction problems via alternating direction methods,” *SIAM J. Sci. Comput.*, vol. 32, pp. 2710–2736, 2010.
- [19] A. Beck and M. Teboulle, “A fast iterative shrinkage-thresholding algorithm for linear inverse problems,” *SIAM J. Imag. Sci.*, no. 1, pp. 183–202, March 2009.
- [20] A. Marquina and S. Osher, “Image super-resolution by TV-regularization and Bregman iteration,” *J. Sci. Comput.*, vol. 37, no. 3, pp. 367–382, 2008.
- [21] W. Yin, S. Osher, D. Goldfarb, and J. Darbon, “Bregman iterative algorithms for ℓ_1 -minimization with applications to compressed sensing,” *SIAM J. Imag. Sci.*, vol. 1, no. 1, pp. 143–168, 2008.
- [22] M. D. Robinson, C. A. Toth, J. Y. Lo, and S. Farsiu, “Efficient Fourier-Wavelet super-resolution,” *IEEE Trans. Image Process.*, vol. 19, no. 10, pp. 2669–2681, 2010.
- [23] F. Sroubek, J. Kamenicky, and P. Milanfar, “Superfast superresolution,” in *Proc. IEEE Int. Conf. Image Process. (ICIP)*, Brussels, Belgium, 2011.
- [24] M. Ebrahimi and E. R. Vrscay, “Regularization schemes involving self-similarity in imaging inverse problems,” in *Proc. 4 th AIP international Conference and the 1st Congress of the IPIA*, 2008.
- [25] K. Zhang, X. Gao, D. Tao, and X. Li, “Single image super-resolution with non-local means and steering kernel regression,” *IEEE Trans. Image Process.*, vol. 21, no. 11, pp. 4544–4556, Nov 2012.
- [26] M. Elad and A. Feuer, “Restoration of a single superresolution image from several blurred, noisy and undersampled measured images,” *IEEE Trans. Image Process.*, vol. 6, no. 12, pp. 1646–1658, 1997.
- [27] S. Farsiu, D. Robinson, M. Elad, and P. Milanfar, “Advances and challenges in super-resolution,” *Int. J. Imaging Syst. Technol.*, vol. 14, no. 2, pp. 47–57, 2004.
- [28] Z. Lin and H.-Y. Shum, “Fundamental limits of reconstruction based superresolution algorithms under local translation,” *IEEE Trans. Patt. Anal. Mach. Intell.*, vol. 26, no. 1, pp. 83–97, 2004.
- [29] J. K. H. Ng, “Restoration of medical pulse-echo ultrasound images,” Ph.D. dissertation, Trinity College, University of Cambridge, 2006.
- [30] M. Elad and A. Feuer, “Restoration of a single superresolution image from several blurred, noisy, and undersampled measured images,” *IEEE Trans. Image Process.*, vol. 6, no. 12, pp. 1646–1658, 1997.
- [31] N. Zhao, A. Basarab, D. Kouamé, and J.-Y. Tourneret, “Joint segmentation and deconvolution of ultrasound images using a hierarchical Bayesian model based on generalized Gaussian priors,” 2015. [Online]. Available: <http://arxiv.org/abs/1412.2813>
- [32] C. P. Robert, *The Bayesian Choice: from Decision-Theoretic Motivations to Computational Implementation*, 2nd ed., ser. Springer Texts in Statistics. New York, NY, USA: Springer-Verlag, 2007.
- [33] A. Gelman, J. B. Carlin, H. S. Stern, D. B. Dunson, A. Vehtari, and D. B. Rubin, *Bayesian data analysis*, 3rd ed. Boca Raton, FL: CRC press, 2013.
- [34] N. Nguyen, P. Milanfar, and G. Golub, “A computationally efficient superresolution image reconstruction algorithm,” *IEEE Trans. Image Process.*, vol. 10, no. 4, pp. 573–583, 2001.

- [35] Q. Wei, N. Dobigeon, and J.-Y. Tourneret, “Fast fusion of multi-band images based on solving a Sylvester equation,” *IEEE Trans. Geosci. and Remote Sens.*, vol. 53, no. 7, pp. 3658–3668, 2015.
- [36] H. A. Aly and E. Dubois, “Image up-sampling using total-variation regularization with a new observation model,” *IEEE Trans. Image Process.*, vol. 14, no. 10, pp. 1647–1659, 2005.
- [37] J. M. Bioucas-Dias, “Bayesian wavelet-based image deconvolution: A GEM algorithm exploiting a class of heavy-tailed priors,” *IEEE Trans. Image Process.*, vol. 15, no. 4, pp. 937–951, 2006.
- [38] J. Ng, R. Prager, N. Kingsbury, G. Treece, and A. Gee, “Wavelet restoration of medical pulse-echo ultrasound images in an EM framework,” *IEEE Trans. Ultrason. Ferroelectr. Freq. Control*, vol. 54, no. 3, pp. 550–568, 2007.
- [39] C. V. Jiji, M. V. Joshi, and S. Chaudhuri, “Single-frame image super-resolution using learned wavelet coefficients,” *Int. J. Imaging Syst. Technol.*, vol. 14, pp. 105–112, 2004.
- [40] M. A. T. Figueiredo and R. D. Nowak, “An EM algorithm for wavelet-based image restoration,” *IEEE Trans. Image Process.*, vol. 12, no. 8, pp. 906–916, 2003.
- [41] R. Fattal, “Edge-avoiding wavelets and their applications,” *ACM Trans. Graph.*, vol. 28, no. 3, pp. 1–10, Aug. 2009.
- [42] S. Roth and M. J. Black, “Fields of experts: a framework for learning image priors,” in *Proc. IEEE Conference on Computer Vision and Pattern Recognition (CVPR)*, 2005, pp. 860–867.
- [43] D. Zoran and Y. Weiss, “From learning models of natural image patches to whole image restoration,” in *Proc. IEEE Int. Conf. Comp. Vision (ICCV)*, Barcelona, Spain, 2011, pp. 479–486.
- [44] H. W. Engl, M. Hanke, and A. Neubauer, *Regularization of inverse problems*. Springer Science & Business Media, 1996, vol. 375.
- [45] O. Féron, F. Orieux, and J.-F. Giovannelli, “Gradient scan Gibbs sampler: an efficient algorithm for high-dimensional Gaussian distributions,” 2015. [Online]. Available: <http://arxiv.org/abs/1509.03495>
- [46] F. Orieux, O. Féron, and J. F. Giovannelli, “Sampling high-dimensional Gaussian distributions for general linear inverse problems,” *IEEE Signal Process. Lett.*, vol. 19, no. 5, pp. 251–254, 2012.
- [47] C. Gilavert, S. Moussaoui, and J. Idier, “Efficient Gaussian sampling for solving large-scale inverse problems using MCMC,” *IEEE Trans. Image Process.*, vol. 63, no. 1, pp. 70–80, 2015.
- [48] W. W. Hager, “Updating the inverse of a matrix,” *SIAM Rev.*, pp. 221–239, 1989.
- [49] Q. Wei, N. Dobigeon, and J.-Y. Tourneret, “Bayesian fusion of multi-band images,” *IEEE J. Sel. Topics Signal Process.*, vol. 9, no. 6, pp. 1–11, 2015.
- [50] Z. Wang, A. C. Bovik, H. R. Sheikh, and E. P. Simoncelli, “Image quality assessment: From error visibility to structural similarity,” *IEEE Trans. Image Process.*, vol. 13, no. 4, pp. 600–612, 2004.
- [51] A. Levin, Y. Weiss, F. Durand, and W. T. Freeman, “Understanding and evaluating blind deconvolution algorithms,” in *Proc. Conf. Computer Vision Patt. Recognition (CVPR)*, Miami, FL, USA, June 2009, pp. 1021–1025.
- [52] S. Boyd, N. Parikh, E. Chu, B. Peleato, and J. Eckstein, “Distributed optimization and statistical learning via the alternating direction method of multipliers,” *Found. Trends Mach. Learn.*, vol. 3, no. 1, pp. 1–122, 2011.
- [53] R. Baraniuk, H. Choi, R. Neelamani, V. Ribeiro, J. Romberg, H. Guo, F. Fernandes, B. Hendricks, R. Gopinath, M. Lang, J. E. Odegard, D. Wei, and J. Jackson, “Rice wavelet toolbox.” [Online]. Available: <http://dsp.rice.edu/software/rice-wavelet-toolbox>